

Effect of Silica Bodies on the Mechanical Behaviour of Oil Palm Empty Fruit Bunch Fibres

Farah Nadia Omar,^a Mohd Afandi P. Mohammed,^{a,*} and Azhari Samsu Baharuddin^{a,b}

The surface of oil palm empty fruit bunch fibres contains embedded silica bodies or protrusions. The mechanical contribution of the protrusions towards the integrity of the fibres is still not clearly investigated. In this work, 2D and 3D finite element simulations on the surface and cross section of the fibres, respectively, were performed. The information for the models was obtained from scanning electron microscopy analysis and mechanical tests for the silica body characteristics and elastic modulus, respectively. Different silica bodies arrangements and the effect of spiked geometry of the silica bodies was investigated using 2D models. Cohesive zone modelling was introduced to simulate damage or debonding between the interface of silica bodies and fibre. A 3D finite element model was later developed consisting of a silica body (sphere) embedded halfway in the matrix. The numerical results showed that the 2D model was sensitive to critical stress compared to silica bodies spiked geometry, arrangement of silica bodies on the fibre surface, and cohesive energy. On the other hand, the results showed that for 3D models with thicknesses larger than 0.2 mm, the effect of the silica bodies on the elasticity of the fibre was not significant.

Keywords: Finite element micromechanics; Cohesive zone modelling; Silica bodies; Fibre interface

Contact information: a: Department of Process and Food Engineering, Faculty of Engineering, Universiti Putra Malaysia, 43400 UPM Serdang, Selangor, Malaysia; b: Institute of Tropical Forestry and Forestry Products (INTROP), Putra Infoport, Universiti Putra Malaysia, 43400 UPM, Serdang, Selangor, Malaysia; *Corresponding author: afandi@upm.edu.my

INTRODUCTION

Oil palm biomass production is expected to increase in the future as a result of the high volume of plantation and milling activities, as well as the requirement for renewable energy sources. As a consequence, a high quantity of oil palm empty fruit bunch (OPEFB) material is being produced (Shuit *et al.* 2009) and utilisation of this readily available and carbonaceous OPEFB is important. The OPEFB are currently being used for biocompost (Bahrin *et al.* 2012) and biocomposites (Nascimento *et al.* 2012), where the focus is on the OPEFB surface, which contains embedded silica bodies (Law *et al.* 2007). Biocompost requires removal of silica bodies from OPEFB fibres using high pressure steam or chemical treatments (Bahrin *et al.* 2012; Shamsudin *et al.* 2012; Yunos *et al.* 2012). The fibres without silica bodies can be easily decomposed (Hamzah *et al.* 2011) because the increase in the surface area allows the enzymatic attack by microorganisms (*i.e.*, fungi) to become more active (Hamzah *et al.* 2011; Bahrin *et al.* 2012). Biocomposites, on the other hand, utilise OPEFB fibres as fillers mixed in a conventional resin (Khalid *et al.* 2008) for products like automotive parts, furniture, and consumer merchandises. The surface of fibres containing silica bodies has been reported to provide more strength to the fibre-resin interface because the silica bodies restrict the

sliding motion between the filler (fibre) and matrix (resin) (d'Almeida *et al.* 2006; Nascimento *et al.* 2012).

An illustration of the microstructure of OPEFB is shown in Fig. 1, consisting of silica bodies on the surface of an oil palm fibre. Notice that the silica bodies are approximately circular-shaped protrusions with an occurrence of spikes (Sreekala *et al.* 1997; Law *et al.* 2007, Omar *et al.* 2014). In addition, the silica bodies are embedded partly in the surface along the longitudinal direction of the fibre. The cell walls are included based on the microscopy cross-sectional images of OPEFB fibres by Shamsudin *et al.* (2012), who reported no trace of silica bodies within the fibre cross-section.

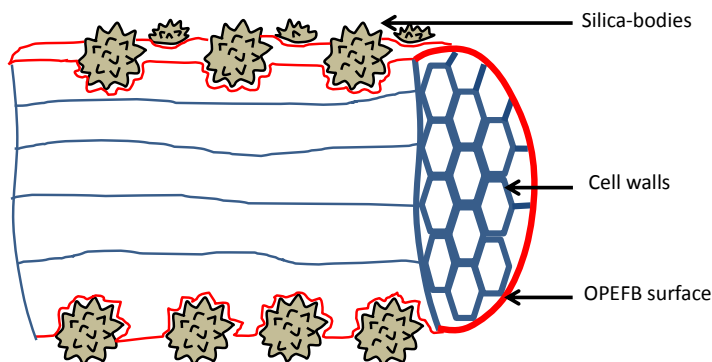


Fig. 1. Cross-section of an oil palm empty fruit bunch fibre (modified from Law *et al.* 2007 and Omar *et al.* 2014)

The applications of OPEFB indicate the need to investigate the contribution of silica bodies to the strength of the fibres, especially on the surface and within the fibre cross section. Note that a preliminary work on the modelling of silica bodies and OPEFB fibre was reported recently by Omar *et al.* (2014), whose work showed that silica bodies influenced the integrity of the fibres due to cohesive debonding. However, the work only considered the surface of the fibres without any consideration for experimental and cross section analysis. Therefore, the objective of this work was to investigate whether silica bodies contribute to the integrity of OPEFB through 2D and 3D micromechanics simulations of the surface and cross section, respectively. The information used for the development of the models was obtained from scanning electron microscopy (SEM) and tensile tests for the characteristics of the silica bodies and elastic modulus, respectively.

EXPERIMENTAL

Materials

The palm species used was *Elaeis guineensis* Jacq. Oil palm empty fruit bunches (OPEFB) were obtained from Besout Palm Oil Mill (Sungkai, Perak, Malaysia) (3°52'59.34''N, 101°16'35.87''E). The samples were physically pressed to remove oil and moisture before being shredded to sizes of 150 to 200 mm. The shredded samples were then kept in a conditioned environment at -20 °C prior to tensile tests and SEM analysis.

Methods

Scanning electron microscopy

Scanning electron microscopy (SEM) analysis was conducted using a scanning electron microscope model S-3400N (Hitachi, Japan) operating at an acceleration voltage of 15 to 25 kV. The OPEFB fibres were cut to sizes ranging from 2 to 5 mm and mounted on an aluminium stub using double-sided adhesive tape. The samples were sputter-coated with platinum prior to morphological assessment (E-1010, Hitachi).

Tensile tests

The length of samples used for tensile tests was fixed at 50 mm. Measurements of the sample diameters were performed using an optical microscope at three different locations, and a mean diameter was calculated. Note that Gunawan *et al.* (2009) reported variations in the OPEFB fibre diameters that ranged from 0.4 mm to 0.72 mm. Gunawan *et al.* (2009) also highlighted that larger diameter fibres of about 0.5 mm and above had large voids or openings within the cross section which weakened the structure of the fibres. Therefore, to make sure that the sample measurements are reliable, only samples with a mean diameter ranging from 0.38 to 0.4 mm were used, which corresponds to ~5% difference. The SEM images of the cross-section area of the fibres (Fig. 3d) show no large voids or openings, which is consistent with the findings by Gunawan *et al.* (2009).

Tensile tests were performed using a TA.XT texture analyser (Stable Micro Systems Ltd., UK) following the preparation method by Yusoff *et al.* (2009). The test configuration consisted of a “C-shaped” paper attached to the fibre with cyanoacrylate adhesive to make sure the fibre stayed aligned (Fig. 2). The sample was then loaded into the texture analyser, where the ends were clamped using a specialised tensile grip. Once the sample was in place between the grip, the paper was cut prior to the tests. The tensile tests were performed by clamping both ends of the sample and pulling them in opposite directions at a constant speed. A load cell of 1 kN was used. The sample deformation was obtained from the cross head displacement of the texture analyser. A total of 20 samples was used throughout the tests.

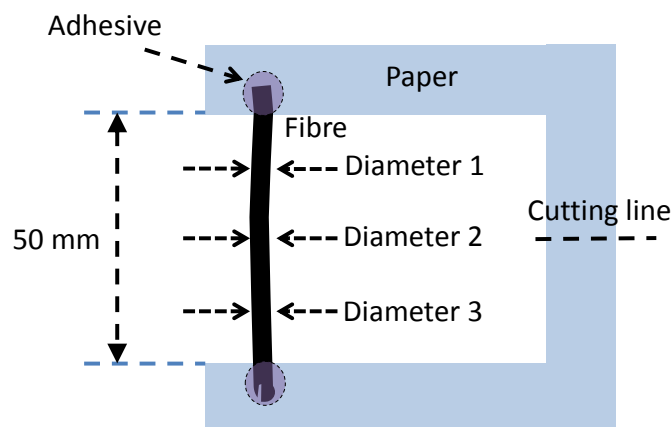


Fig. 2. Tensile test configuration of an oil palm fibre consisting of “C-shaped” paper to hold the fibre

From the force and displacement results obtained from the tensile tests, the true stress, σ , was measured using the following equation,

$$\sigma = \frac{4Fl}{\pi D^2 l_0} \quad (1)$$

where F is the applied force obtained from the texture analyser, D is the diameter of the sample, and l and l_0 are the deformed and original lengths of the sample, respectively. Note that Eq. 1 assumes a cylindrical sample based on the diameter measurements of the fibre at three different locations along the fibre length (Fig. 2). Values were within $\pm 1\%$ difference for all the fibres tested. The true strain (log strain), ε , was calculated as follows:

$$\varepsilon = \ln\left(\frac{l}{l_0}\right) \quad (2)$$

RESULTS AND DISCUSSION

Microstructure of OPEFB

The SEM images of an undeformed OPEFB fibre surface show that silica bodies were partly embedded (Figs. 3a and 3b). The geometry of the protrusions was circular with the occurrence of spikes (Fig. 3c), which is consistent with the findings of Law *et al.* (2007) and Shamsudin *et al.* (2012). The silica bodies were dispersed on the surface of the fibre in approximately random and aligned arrangements, as shown in Figs. 3a and 3b, respectively. A similar aligned arrangement of silica bodies was observed by Sreekala *et al.* (1997) and Isroi *et al.* (2012), and random arrangement was observed by Hamzah *et al.* (2011) and Bahrin *et al.* (2012).

The cross-section image of an undeformed OPEFB sample in Fig. 3d shows cell-walls with thicknesses of about 5 μm and cell sizes of 5 to 20 μm . In comparison, Fig. 3e shows cell wall structures for a sample after fracture deformation from the uniaxial tension test. One can see the difference between Figs. 3d and 3e, where the latter shows torn-out fibres compared to the former. In both images, no occurrences of silica bodies could be observed in the cell walls, which is in agreement to the findings by Shamsudin *et al.* (2012). Finally, Fig. 3f shows the image of the sample surface after a tensile test with some craters observed due to the absence of silica bodies.

Tensile Tests of OPEFB Fibres

Figure 4 shows an example of a tensile test result, where the stress-strain curve are separated into elastic, plastic, and fracture regions. In the first region where strain was less than about 0.03, damage within the microstructure of the fibre was thought to be minimal and the stress-strain curve showed linear elastic behaviour. For strains beyond 0.03, the plastic region was observed where Omar *et al.* (2014), through a numerical work, suggested that the region is related to the debonding of the silica-body and OPEFB fibre interface. Finally, in the fracture region, fracture or total failure of OPMF was observed from the sudden drop of stress.

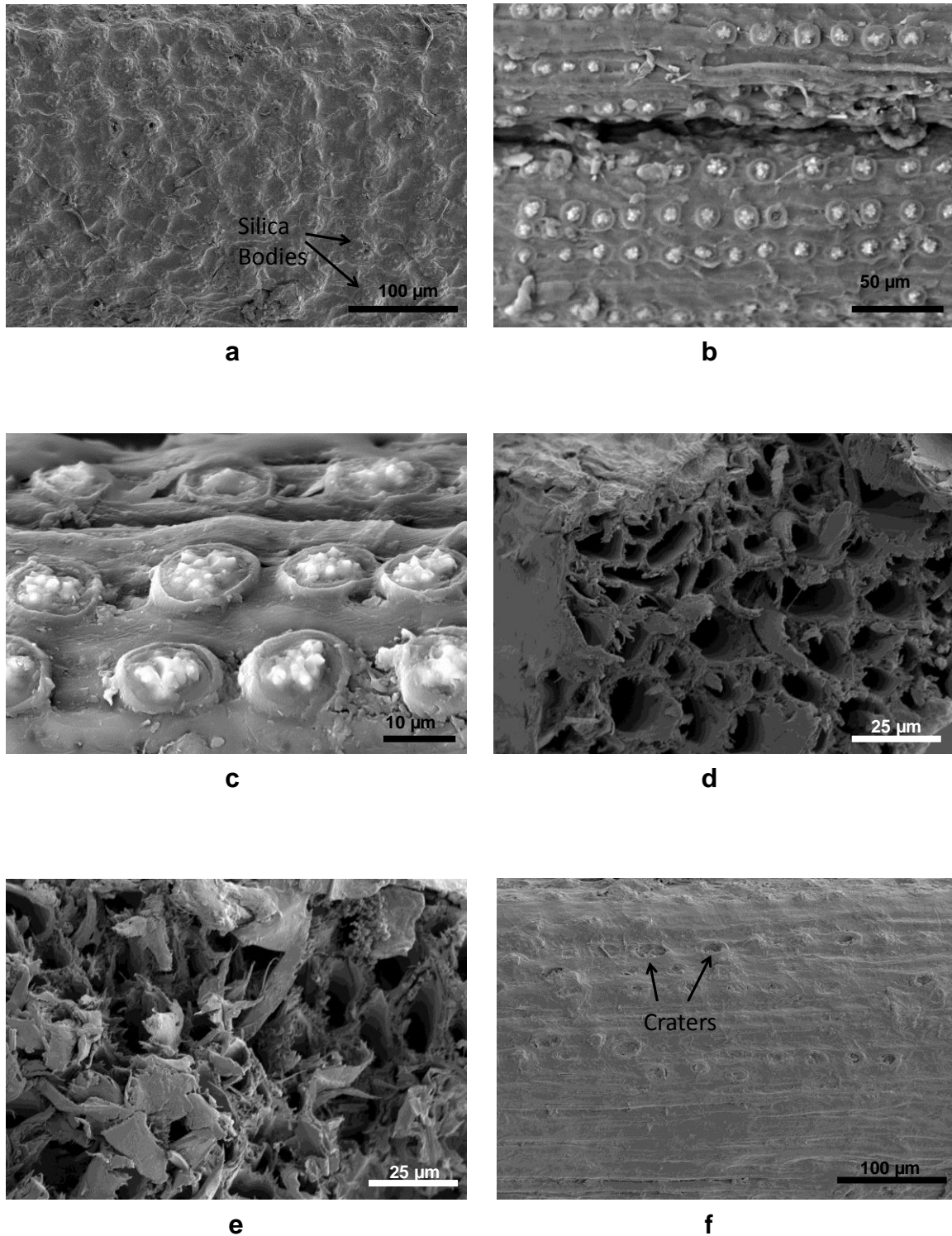


Fig. 3. SEM images of OPEFB fibre and silica bodies. (a) Random arrangement of silica bodies on the fibre surface, (b) aligned arrangement of silica bodies, (c) close-up view of silica bodies, (d) cross-section of OPEFB (undeformed sample), (e) cross-section at fractured region, and (f) sample surface after fracture with some silica bodies absent (craters)

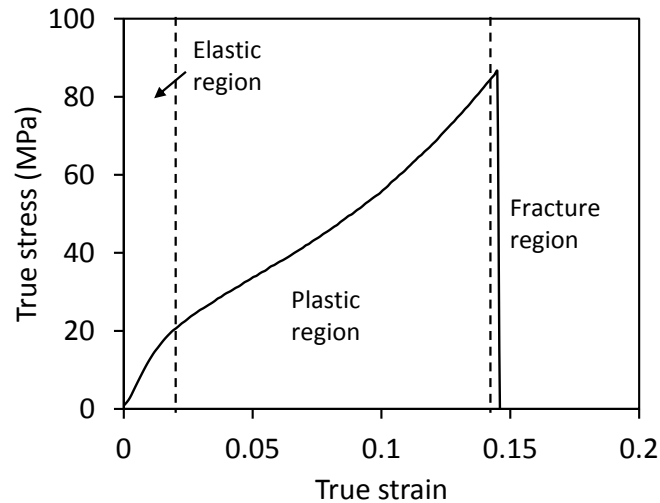


Fig. 4. Stress strain curve from a tensile test result

The average values of elastic modulus, yield stress, failure stress, and failure strain are shown in Table 1. These values can be compared to the test results obtained by Yusoff *et al.* (2009), where elastic modulus, yield stress, failure stress, and failure strain were measured as 1.7 GPa, ~20 MPa, ~45 MPa, and ~0.13, respectively.

Table 1. Average Values from Tensile Tests

Elastic modulus (MPa)	Yield stress (MPa)	Fracture stress (MPa)	Fracture strain
995.9 (120)	25.8 (3)	74.4 (7)	0.16 (0.04)

Standard deviation denoted in parentheses

The initial elastic modulus of OPEFB was approximately 1 GPa (Table 1). This value was smaller than the elastic moduli reported in previous work (1.7 GPa by Yusoff *et al.* (2009) and 5 GPa by Gunawan *et al.* (2009)) and could be due to planting condition and geometry differences of the samples. Yusoff *et al.* (2009) and Gunawan *et al.* (2009) reported increases of elastic modulus with reduction of the diameter of the fibres. Gunawan *et al.* (2009) showed that this is due to large voids or openings in the cross section of OPEFB which cause a non-uniform cross section area. Because the fibres used in this work have no large voids and the sample dimensions were controlled, the modulus obtained from Table 1 is used in the later sections.

2D Micromechanical Model

A micromechanical finite element model was developed to simulate the surface of OPEFB fibre and silica bodies (Figs. 3a to 3c). A 2D multi-particle model, which consisted of 20 particles representing silica bodies surrounded by a fibre as the matrix, was produced using the commercial finite element software Abaqus version 6.9 (Hibbit Karlsson and Sorensen; Providence, RI) and the Abaqus/Standard procedure was followed (Abaqus 2009). The particles were dispersed in the fibre matrix as aligned, clustered, and random arrangements. The model with an aligned particles arrangement

had space between the particles in x and y directions of about 30 μm , whereas in the clustered particles model, the space between the particles was set at 28 to 35 μm within each cluster. The random particles model was produced such that the particles were scattered in the matrix without causing the particles to overlap. An example of the random particles model is shown in Fig. 5a.

It should be noted that the occurrence of spikes in the silica bodies as shown in Fig. 3c needs to be investigated in the model. However, to include the geometry of spikes in the circular model using a number of particles would cause convergence and mesh distortion problems during a finite element simulation process. An alternative is to create a model consisting of a single particle that has a circular geometry with spikes surrounded by a fibre matrix with an area fraction similar to those of the multi-particles model. This approach is widely used in micromechanics (Mishnaevsky 2007) and was applied in this work following a similar method by Omar *et al.* (2014). A single-particle model was produced with a geometry consisting of 10 spikes (Fig. 6b) where any sharp edge on the spikes was fine-tapered to improve the convergence of the finite element modelling results. It was observed that a model with a similar area fraction (15%) and a different numbers of spikes (*i.e.*, 5, 10, and 20 spikes) yielded similar results with a ± 1 difference (results not shown). A similar finding was also reported by Omar *et al.* (2014). Therefore, only results of the model with 10 spikes will be shown in the remainder of this work.

The silica body area fraction for the single-particle and multi-particles models was obtained from at least eight SEM images at different magnifications and was set at $15\% \pm 4$. This was performed using ImageJ software (Rasband 2012) by converting the SEM images into binary images (black and white) and counting the area difference between the black and white areas. Note that the silica bodies volume fraction was not used in this section since the volume fraction was not uniform across the cross-section (see Fig 3d). Further analysis on this is provided later in the 3D modelling section. To simulate the surface of OPEFB, 2D plane stress elements (CPS element type in Abaqus) were selected to represent the thin surface of silica bodies and OPEFB fibre. A quasi-static time step was used throughout the analysis in Abaqus.

The model was loaded under uniaxial tension at a constant speed of 1 mm/s. The following boundary conditions were used for uniaxial tension,

$$\begin{aligned}u(0,0) &= v(x,0) = 0 \\v(x,b) &= \delta\end{aligned}\tag{3}$$

where δ is the applied displacement which is $\delta > 0$ under uniaxial tension, u and v are displacements in the x and y direction, respectively, b is the length of the model, and $(0,0)$ is the origin coordinate at the lower left corner of the model (Fig. 5). Note that no periodic boundary conditions were specified in the models since it was found that a very similar stress-strain curve was obtained when a comparison was performed between the simulation results with and without periodic boundary conditions. Typical differences between results were less than 1%. Periodic boundary conditions in this case referred to the models undergoing similar displacements on the vertical sides (stretching direction) of the model geometry.

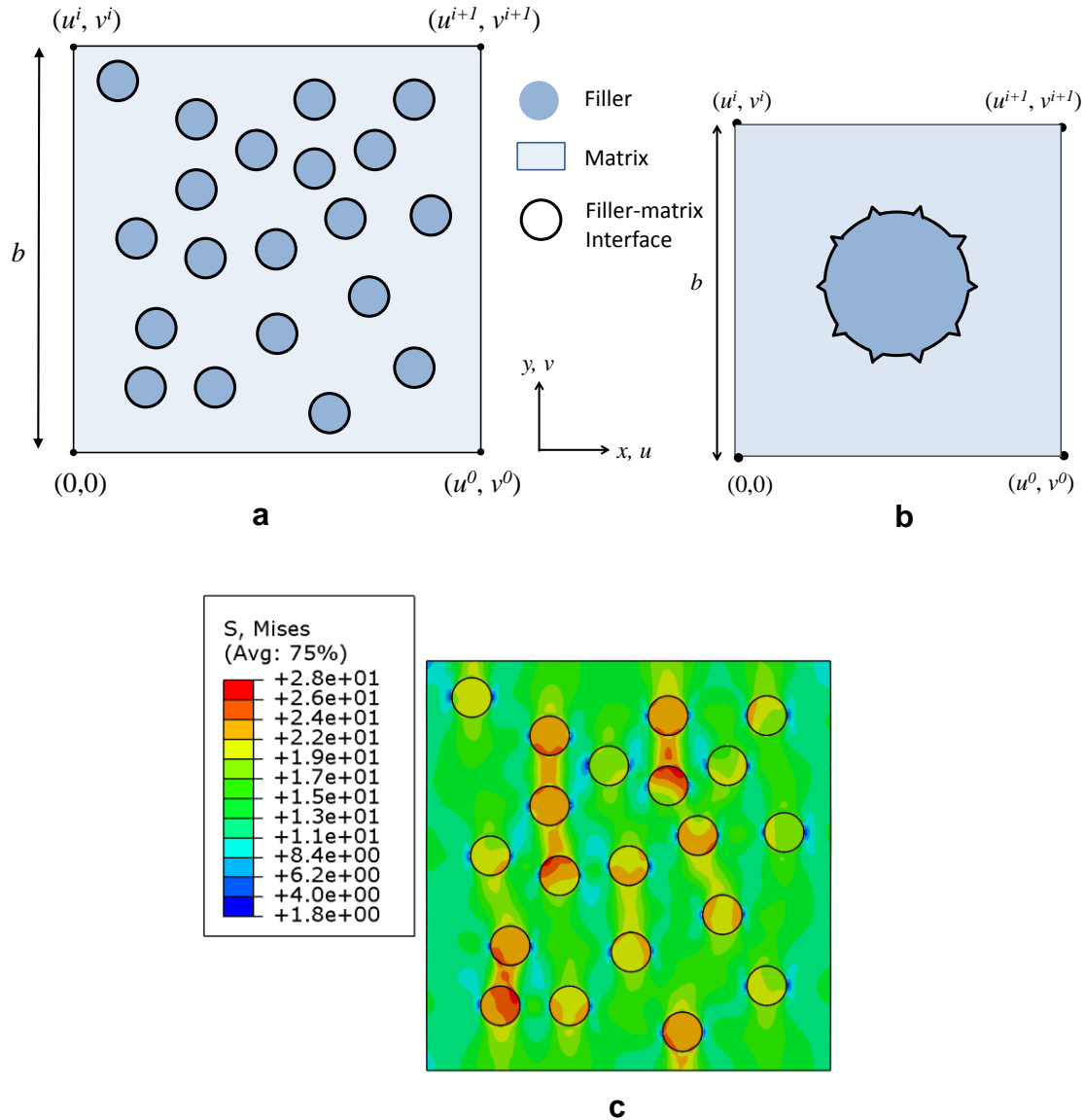


Fig. 5. 2D micromechanics models of OPEFB surface. (a) Random arrangement multi-particles model, (b) a single particle with 10 spikes, and (c) a simulation image of a multi-particles model where the scale is in MPa (von-Mises stress)

Cohesive zone modelling (CZM) was introduced to simulate the damage or debonding between the interface of silica bodies and OPEFB. Cohesive contact was defined between the interface as an option in Abaqus (2009). In the model, the particles were initially bonded to the fibre, where a perfect bonding was assumed. Cohesive zone modelling was then introduced using the traction-separation law shown in Fig. 6.

The three modes of failure in the CZM are usually referred to as opening Mode I (normal tension mode), Mode II (shear mode), or Mode III (out of plane shear mode) (Camanho and Davila 2002; Magnusson and Ostlund 2013). In this work, only Mode I (normal tension mode) was considered to simplify the model, since only tensile tests of OPEFB were available.

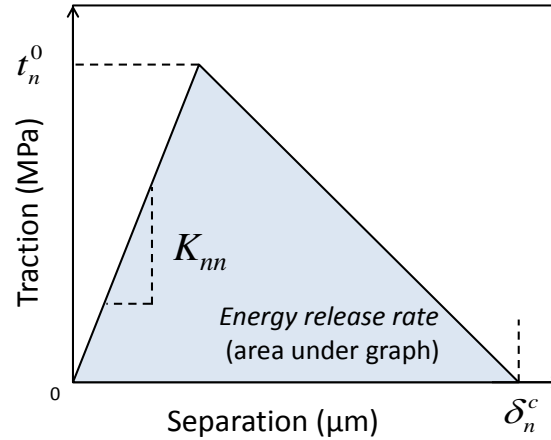


Fig. 6. Traction versus separation of the cohesive zone model under Mode I (normal tension mode)

The traction versus separation law used to model the cohesive damage under Mode I is described as,

$$t_n = K_{nn} \delta_n \quad (4)$$

where t_n is the nominal traction stress, K_{nn} is the normal coefficient, and δ_n is the normal separation. The traction versus separation law for Mode I damage can be separated into two regions (Camanho and Davila 2002; Abaqus 2009) as shown in Fig. 6. In the first region, the traction-separation graph is linear elastic and is described using Eq. 4. In the second region, critical normal stress (t_n^o) occurs and debonding is initiated. Damage or debonding is activated in terms of a maximum stress criterion and is expressed as,

$$\max \left\{ \frac{\langle t_n \rangle}{t_n^o} \right\} = 1 \quad (5)$$

where the symbol $\langle t_n \rangle$ represents the Macaulay bracket, defined as,

$$\langle t_n \rangle = \frac{1}{2} (|t_n| + t_n) \quad (6)$$

implying that damage or debonding is not initiated in compression. Progressive damage in the interface occurs until complete failure or debonding. The damage evolution law describes the rate at which the cohesive stiffness is degraded after the damage initiation criterion is reached. The energy that is dissipated as a result of the damage process, *i.e.*, the cohesive energy (G_c), is equal to the area under the traction-separation curve in Fig. 6 (*i.e.*, $G_c = t_n^o \delta_n^c / 2$).

The material parameters used in the 2D models are shown in Table 2. The properties of the particles have been described by Nordin *et al.* (2013), who reported trace of silica through an energy dispersive X-ray spectroscopy (EDS) analysis on a protrusion or silica body of an oil palm fibre. Due to the results of this study (by assuming the protrusions composition is mainly silica), an elastic modulus of 70 GPa was used under the assumption that the particles were silicon dioxide. The elastic modulus for

OPEFB fibre was obtained from the elastic region of the tensile test results in Table 1 and was set at 1 GPa. This value was also based on calculations using the rule of mixtures for both silica bodies and OPEFB fibre proposed by Omar *et al.* (2014), where it was found that the calculated volume fraction of the silica bodies was very small compared to the total fibre volume. This is because the particles are only available on the fibre surfaces.

Table 2. Materials Parameters Used in the Micromechanics Models of OPEFB

Silica body elastic modulus, E_f (GPa)	70
OPEFB elastic modulus, E_m (GPa)	1.0
CZM normal coefficient, K_{mn} (GPa/m)	1×10^8
CZM critical normal stress, t_n^0 (MPa)	8.0
CZM cohesive energy, G_c (kJ/m)	0.1

In the no-damage model, the interface between silica bodies and fibre was set to be perfectly bonded. Cohesive zone modelling was then activated in the damage model to simulate the debonding of silica bodies and the fibre interface. All the material model parameters of CZM were set to be physically reasonable to the OPEFB behaviour and numerically converged when simulated. The material model parameters for CZM as shown in Table 2 were obtained as follows. The normal coefficient, K_{mn} , was set to be high to prevent interpenetration of the element faces and to prevent artificial compliance from being introduced into the model (Song *et al.* 2008). The critical normal stress value was estimated from the deviation of the tensile stress-strain curve from the elastic region as shown in Fig. 4. Finally, the cohesive energy, $G_c = 0.1 \text{ kJ/m}^2$ (kJ/m^2), was estimated by setting the critical separation, δ_n^c , to $25 \mu\text{m}$, which is in the range of the diameter of a silica body (10 to $25 \mu\text{m}$). The modelling results and an example of a simulation image are shown in Figs. 7 and 5c, respectively.

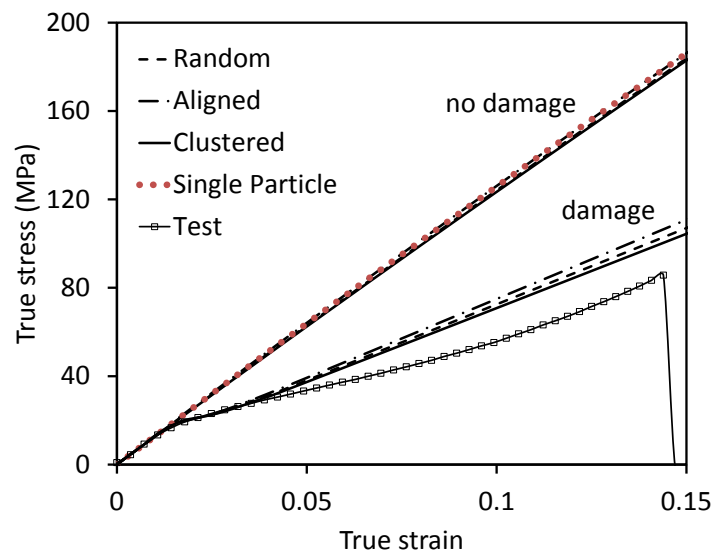


Fig. 7. Modelling results of 2D micromechanics models, where the curves “Random”, “Aligned”, and “Clustered” refer to the arrangement of silica bodies in the models

Note that the result of the single-particle model with damage terminated prematurely at a strain of about 0.02, where CZM was not activated within the range. However, the single-particle model without damage shows a similar result to the model with different particles arrangements (Fig. 7). Deviation of the stress-strain curve is clearly shown by the models with CZM activated (with damage) when compared to those without damage. In addition, similar results are obtained using different particles arrangements.

A parametric study was performed to investigate the sensitivity of the CZM parameters to stress-strain curves. The cohesive damage parameters were first set to the values in Table 2. The critical stress was then kept constant while varying the cohesive energy in a parametric study for case 1, and *vice versa* for case 2. Critical stress, t_n^0 , values of 8, 40, and 80 MPa were used as varying parameters for case 1 (while setting $G_c = 0.1$ kN/m), whereas cohesive energy, G_c , values of 0.01, 0.1, and 1 kN/m were used for case 2 (while setting $t_n^0 = 8$ MPa). The random arrangement model was used for the parametric study.

The parametric study results are shown in Figs. 8a and 8b for case 1 and case 2, respectively. It can be seen that once the critical stresses were activated (case 1), different stress-strain curves were obtained when compared to the no-damage model. In comparison, the parametric study results for case 2 show that the model does not differ given cohesive energy values of 0.1 kN/m and 1 kN/m. These results highlight the issue of non-uniqueness of the cohesive energy values obtained using CZM, which has been discussed by Mohammed *et al.* (2013).

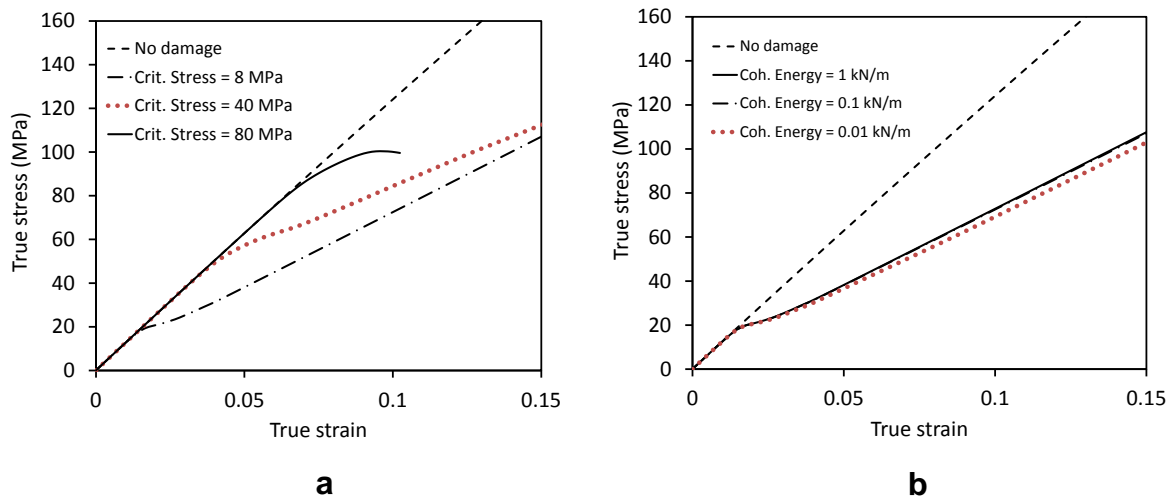


Fig. 8. Parametric study of 2D models with CZM. (a) Results under different critical stress, t_n^0 (case 1) and (b) results under different G_c (case 2). The multi-particle model with random arrangement is used

It is possible that anisotropic or orthotropic behaviour could be observed within the matrix; this has been reported for other lignocellulosic materials like wood (Qing and Mishnaevsky 2009a,b). One can see this from the OPEFB image in Fig. 3, which suggests that the fibre was aligned in a longitudinal direction. To investigate this, an anisotropic material model is included in the 2D multi-particles model. For plane stress elements (2D model), the simplified theory of anisotropy can be described as follows,

$$\begin{bmatrix} \sigma_{xx} \\ \sigma_{yy} \\ \tau_{xy} \end{bmatrix} = \begin{bmatrix} E_x & -\nu_{xy}E_x & 0 \\ -\nu_{xy}E_x & E_y & 0 \\ 0 & 0 & G_{xy} \end{bmatrix} \begin{bmatrix} \varepsilon_{xx} \\ \varepsilon_{yy} \\ \gamma_{xy} \end{bmatrix} \quad (6)$$

where σ_{xx} and σ_{yy} are the normal stresses in the principal directions (refer to Fig. 5 for the principal directions), τ_{xy} is the shear stress, and E_x and E_y are the elastic moduli. The other parameters, G_{xy} and ν_{xy} , are the shear modulus and Poisson's ratio, respectively, which were set as $G_{xy} = E_y/2(1+\nu_{xy}) = 333.3 \text{ MPa}$ and $\nu_{xy} = 0.5$ for an incompressible material assumption.

It would be interesting to investigate the shear modulus and Poisson's ratio of OPEFB in the future using an experimental method. The anisotropic simulations were performed as follows. First, the modulus E_y was set to be the same as the isotropic model (1 GPa). Then, E_x was set at half and one quarter the value of E_y , where these models were called Anisotropy A (0.5 GPa) and Anisotropy B (0.33 GPa), respectively. In a different case, the modulus E_x was fixed at 1 GPa and E_y was set at half and one quarter the value of E_x , where these models were called Anisotropy C (0.5 GPa) and Anisotropy D (0.33 GPa), respectively.

Similar CZM parameters were applied to the models as in Table 2. The results are shown in Fig. 9, which indicate that the anisotropic models are sensitive towards the elastic modulus in the loading direction. Note that the simulation results using Anisotropy C and Anisotropy D models show similar findings to those obtained by Omar *et al.* (2014) using a single particle model.

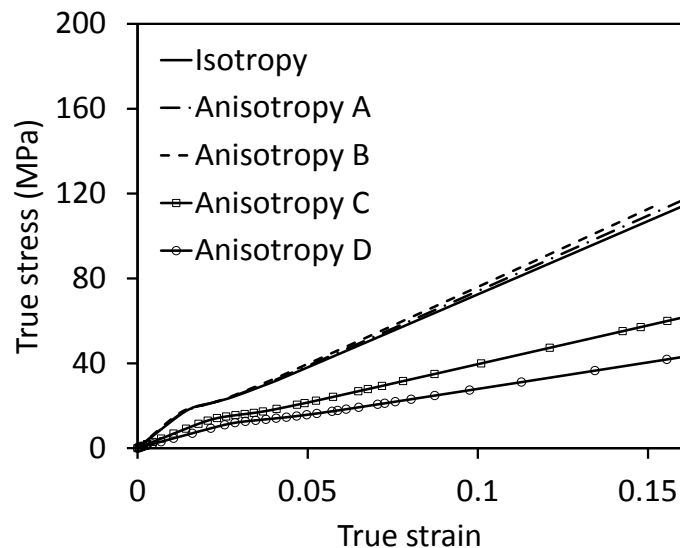


Fig. 9. 2D modelling results using anisotropy material models and CZM

3D Micromechanical Model

The 2D modelling results in the previous section focused on the surface of OPEFB. However, it should be noted that silica bodies are only available on the surface of the fibre and that the effects of silica bodies on elasticity and damage along the fibre

cross-section are not known. To investigate this, a 3D finite element model was developed consisting of a silica body (sphere) embedded halfway in the matrix as shown in Fig. 10.

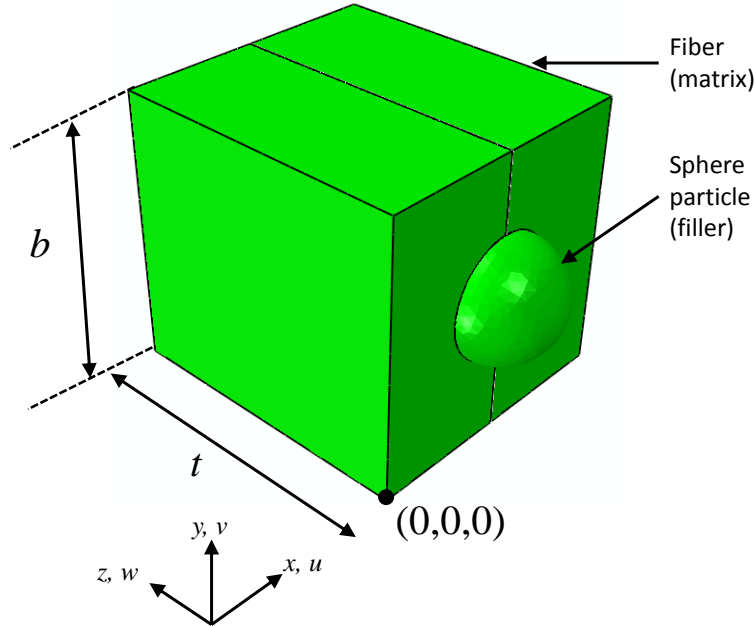


Fig. 10. 3D finite element model of silica body (sphere) embedded halfway in the matrix

A 3D element type C3D4 linear tetrahedron was specified to mesh the model geometry. The material properties in Table 2 were applied to simulate debonding in a similar way as the 2D models in previous section. The boundary conditions for the model under uniaxial tension are as follows,

$$\begin{aligned} u(0,0,z) = v(x,0,z) = w(x,0,t) &= 0 \\ v(x,b,z) &= \delta \end{aligned} \quad (7)$$

where δ is the applied displacement, u , v , and w are displacements in the x , y , and z directions, respectively, b and t are the length and thickness of the model, respectively, and $(0,0,0)$ is the origin coordinate of the model. The thickness, t , in this case was assumed to be the radius of a single OPEFB fibre and was initially set at 0.2 mm. A quasi-static time step was used in the analysis and the Abaqus/Standard procedure was followed.

The results are shown in Fig. 11 and can be compared to the results using 2D models which are shown in Fig. 7. When CZM is activated, a slight deviation from the elastic region was observed for models with different thicknesses. The difference was much less significant in the 3D model results than in the 2D model results shown in Fig. 7. Unfortunately, the simulation of the model with damage (CZM) terminated early at a strain of about 0.05 before further results could be obtained.

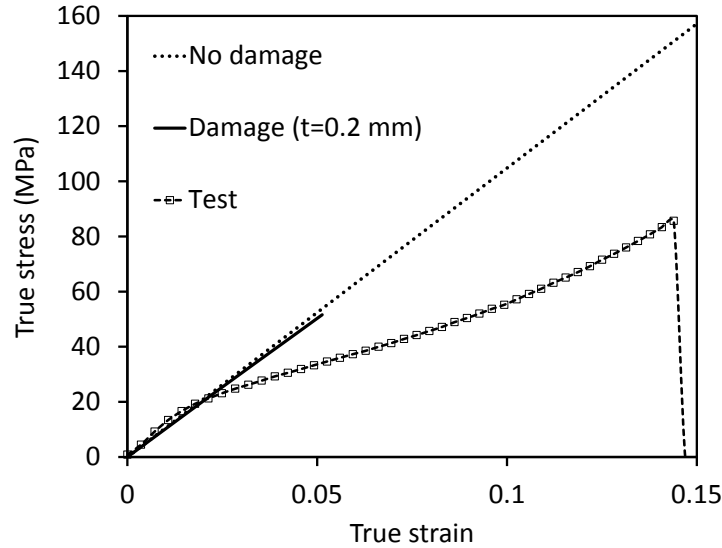


Fig. 11. Comparison of the 3D models and the experimental result

To further investigate the 3D models, the thickness of the matrix, t , was varied in the z direction from 0.03 to 0.3 mm to analyse the effect of fibre thickness on the elasticity of the fibre-protrusion system. The results are shown in Figs. 12a and 12b for the case of a perfect silica body and fibre interface (no-debonding) and with CZM activated (debonding), respectively. In Fig. 12a, it was noticed that for thicknesses larger than 0.2 mm, the effect of the silica-body on the elasticity of the fibre was not significant. This indicates that the modulus obtained from the tests on bulk fibres with an average radius of about 0.2 mm (Table 1) is sufficient to characterise the fibre-protrusion system studied here. Furthermore, because the 3D model gives more realistic results than the 2D model (since the 3D model considers the cross section of the fibre), one can see that the effect of silica bodies on the elasticity of the fibre is not significant, especially for fibres larger than 0.2 mm.

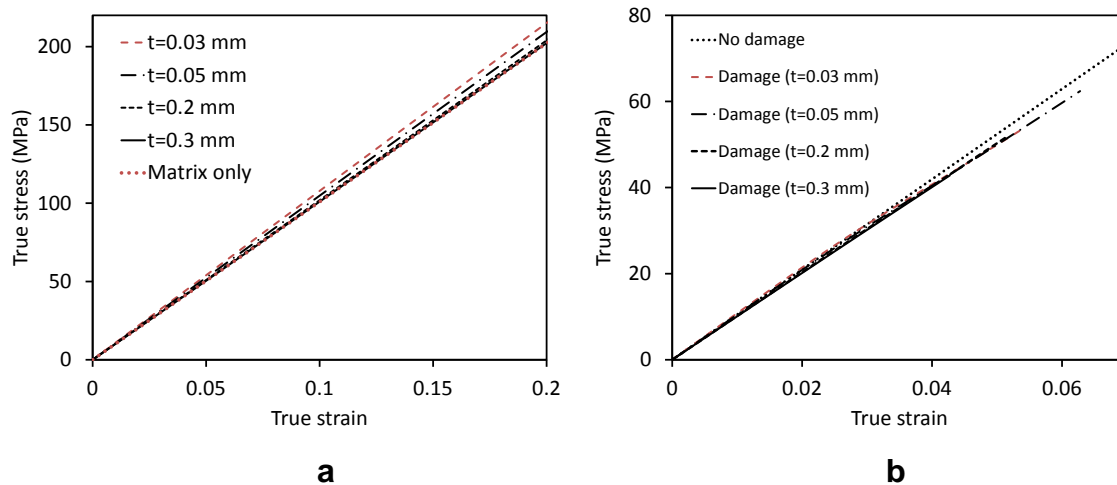


Fig. 12. 3D finite element results for different matrix thicknesses, t . (a) Perfect silica-body and fibre interface and (b) results with CZM activated using parameters in Table 2

A further numerical analysis was conducted by adding a cell wall opening to the 3D model, as shown in the inset of Fig. 13. The thickness of the cell wall was set at 0.005 mm, and the opening size was set at 0.02 mm, as approximated values from cell wall images in Fig. 3d. The total thickness, t , for the whole model was 0.04 mm. The modelling result was then compared to those without cell walls as presented in Fig. 13.

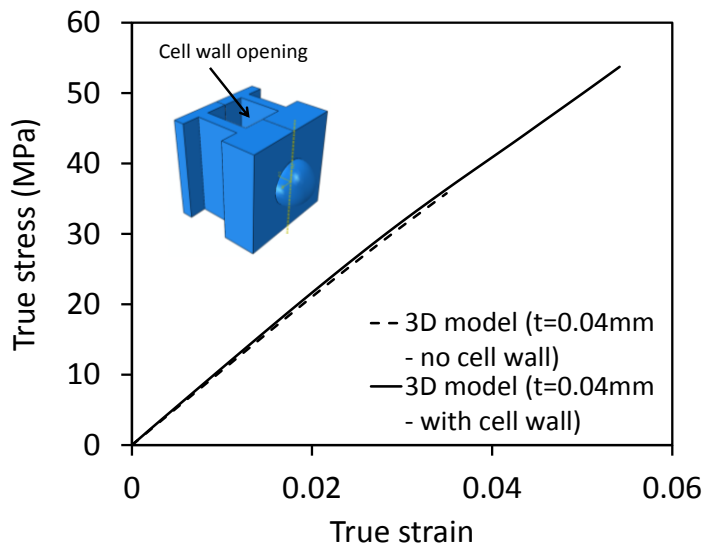


Fig. 13. Modelling results without and with the inclusion of cell wall opening

Similar results were obtained from both models, highlighting that different mechanisms within the fibres might be responsible for the plastic region of stress-strain curves shown in Fig. 4 in addition to the silica bodies and fibre interface damage. This includes mechanisms of damage reported for other lignocellulosic materials such as damage to cell wall sublayers and at the lignin-hemicellulose-cellulose interface. Cell wall damage involves interaction between different sublayers of cell walls, which can be anisotropic in nature (Salmén 2004). The anisotropic behaviour of the cell walls in lignocellulosic material (wood) has been investigated by Qing and Mishnaevsky (2009a) using a finite element model, whereas experimental work was performed by Burgert (2006). On the other hand, the cellulose-hemicellulose interface has recently been investigated numerically by Adler and Buehler (2013), where they suggested a stick-slip motion of the interface. In addition, Qing and Mishnaevsky (2009b) and Flores and Friswell (2012) modelled cellulose as a cylindrical material surrounded by lignin and hemicellulose.

It is worth noting that for composites application, untreated fibres have the advantage of having silica bodies to prevent sliding between the fibre filler and resin matrix (Nascimento *et al.* 2012). Otherwise, pre-treated fibres with the absence of silica bodies (Shamsudin *et al.* 2012) can improve the adhesion between filler and matrix through better bonding or interface (Kalia *et al.* 2009). However, it should be noted that pre-treatment of lignocellulosic fibres like OPEFB can cause degradation of the fibre components, namely cellulose, hemicellulose, and lignin (Isroi *et al.* 2012). This we believe can cause significant damage to the fibres as the lignin and hemicellulose bind the cellulose fibrils together and provide structural integrity to the lignocellulosic fibres (Adler and Buehler 2013). Note that for OPEFB, it was reported that the composition of cellulose, hemicellulose, and lignin are 47.6%, 28.1%, and 13.1%, respectively

(Baharuddin *et al.* 2012). These further highlight the complexity of OPEFB, which is believed to have similarities to wood materials, but with the special feature of having silica bodies embedded in the surface of the fibres.

CONCLUSIONS

1. Investigation of tensile tests, SEM analysis, and finite element modelling of OPEFB were performed in this work. The SEM images showed that silica bodies were observed only on the surface of the OPEFB fibre, whereas the fibre cross section consisted of cell wall structures.
2. The 2D and 3D finite element micromechanics models were developed using silica bodies as particles surrounded by OPEFB fibre. Cohesive zone modelling (CZM) was introduced to model damage or debonding between the interface of silica bodies and fibre. Different silica body arrangements on the fibre were investigated in the 2D model, namely random, aligned, and clustered.
3. The 2D modeling results suggested that the silica bodies and the fibre interface can damage the OPEFB. In particular, the 2D models were sensitive to critical stress compared to silica bodies' spiked geometry, the arrangement of silica bodies on the fibre surface, and cohesive energy. However, the 3D modeling results showed that for thicknesses larger than 0.2 mm, the effect of silica bodies on the elasticity of the fibre is not significant.

ACKNOWLEDGEMENTS

The authors would like to thank Lee Xiao Fen from the Department of Process and Food Engineering, Universiti Putra Malaysia for performing the experimental work. Funding for this work is contributed by the Knowledge Transfer Programme grant (KTP 6228118) and Fundamental Research Grant Scheme (FRGS/2/2013/TK04/UPM/02/7) under the Malaysian Ministry of Education and Universiti Putra Malaysia.

REFERENCES CITED

- Abaqus (2009). *User Manual ver. 6.9*, Hibbitt Karlsson and Sorensen, Providence, RI.
- Adler, D. C., and Buehler, M. J. (2013). "Mesoscale mechanics of wood cell walls under axial strain," *Soft Matter* 9(29), 7138-7144. DOI: 10.1039/c3sm50183c
- Baharuddin, A. S., Md-Yunos, N. S. H., Nik-Mahmud, N. A., Zakaria, R., and Md-Yunos, K. F. (2012). "Effect of high-pressure steam treatment on enzymatic saccharification of oil palm empty fruit bunches," *BioResources* 7(3), 3525-3538.
- Bahrin, E. K., Baharuddin, A. S., Ibrahim, M. F., Razak, M. N. A., Sulaiman, A., Abd-Aziz, S., Hassan, M. A., Shirai, Y., and Nishida, H. (2012). "Physicochemical property changes and enzymatic hydrolysis enhancement of oil palm empty fruit bunches treated with superheated steam," *BioResources* 7(2), 1784-1801.
- Burgert, I. (2006). "Exploring the micromechanical design of plant cell walls," *Am. J. Bot.* 93(10), 1391-1401. DOI: 10.3732/ajb.93.10.1391

- Camanho, P. P., and Davila, C. G. (2002). "Mixed-mode decohesion finite elements for the simulation of delamination in composite materials," *NASA Technical Report*, NASA/TM-2002-211737.
- d'Almeida, J. R. M., Aquino, R. C. M. P., and Monteiro, S. N. (2006). "Tensile mechanical properties, morphological aspects and chemical characterization of piassava (*Attalea funifera*) fibers," *Compos. Part A: Appl. Sci. Manuf.* 37(9), 1473-1479. DOI: 10.1016/j.compositesa.2005.03.035
- Flores, E. I. S., and Friswell, M. I. (2012). "Multi-scale finite element model for a new material inspired by the mechanics and structure of wood cell-walls," *J. Mech. Phys. Solids* 60(7), 1296-1309. DOI: 10.1016/j.jmps.2012.03.007
- Gunawan, F. E., Homma, H., Brodjonegoro, S. S., Hudin, A. B., and Zainuddin, A. (2009). "Mechanical properties of oil palm empty fruit bunch fiber," *J. Solid Mech. Mater. Eng.* 3(7), 943-951. DOI: 10.1299/jmmp.3.943
- Hamzah, F., Idris, A., and Shuan, T. K. (2011). "Preliminary study on enzymatic hydrolysis of treated oil palm (*Elaeis*) empty fruit bunches fibre (EFB) by using combination of cellulase and β 1-4 glucosidase," *Biomass Bioenerg.* 35(3), 1055-1059. DOI: 10.1016/j.biombioe.2010.11.020
- Isroi, Ishola, M. M., Millati, R., Syamsiah, S., Cahyanto, M. N., Niklasson, C., and Taherzadeh, M. J. (2012). "Structural changes of oil palm empty fruit bunch (OPEB) after fungal and phosphoric acid pretreatment," *Molecules* 17(12), 14995-15012. DOI: 10.3390/molecules171214995
- Kalia, S., Kaith, B. S., and Kaur, I. (2009). "Pretreatments of natural fibers and their application as reinforcing material in polymer composites-A review," *Polym. Eng. Sci.* 49(7), 1253-1272. DOI: 10.1002/pen.21328
- Khalid, M., Ratnam, C. T., Chuah, T. G., Ali, S., and Choong, T. S. Y. (2008). "Comparative study of polypropylene composites reinforced with oil palm empty fruit bunch fiber and oil palm derived cellulose," *Mater. Des.* 29(1), 173-178. DOI: 10.1016/j.matdes.2006.11.002
- Law, K. N., Daud, W. R. W., and Ghazali, A. (2007). "Morphology and chemical nature of fiber strands of oil palm empty-fruit-bunch (OPEFB)," *BioResources* 2(3), 351-362.
- Magnusson, M. S., and Ostlund, S. (2013). "Numerical evaluation of interfibre joint strength measurements in terms of three-dimensional resultant forces and moments," *Cellulose* 20(4), 1691-1710. DOI: 10.1007/s10570-013-9939-x
- Mishnaevsky, L. (2007). *Computational Mesomechanics of Composites: Numerical Analysis of the Effect of Microstructures of Composites on Their Strength and Damage Resistance*, John Wiley and Sons, Chichester.
- Mohammed, M. A. P., Tarleton, E., Charalambides, M. N., and Williams, J. G. (2013). "Mechanical characterization and micromechanical modeling of bread dough," *J. Rheol.* 57(1), 249-272. DOI: 10.1122/1.4768463
- Nascimento, D. C. O., Ferreira, A. S., Monteiro, S. N., Aquino, R. C. M. P., and Kestur, S. G. (2012). "Studies on the characterization of piassava fibers and their epoxy composites," *Compos. Part A: App. Sci. Manuf.* 43(3), 353-362. DOI: 10.1016/j.compositesa.2011.12.004
- Nordin, N. I. A., Ariffin, H., Andou, Y., Hassan, M. A., Shirai, Y., Nishida, H., Yunus, W. M. Z. W., Karuppuchamy, S., and Ibrahim, N. A. (2013). "Modification of oil palm mesocarp fiber characteristics using superheated steam treatment," *Molecules* 18(8), 9132-9146. DOI: 10.3390/molecules18089132

- Omar, F. N., Mohammed, M. A. P., and Bahruddin, A. S. (2014). "Microstructure modelling of silica bodies from oil palm empty fruit bunch (OPEFB) fibres," *BioResources* 9(1), 938-951.
- Qing, H., and Mishnaevsky, L. (2009a). "3D hierarchical computational model of wood as a cellular material with fibril reinforced, heterogeneous multiple layers," *Mech. Mater.* 41(9), 1034-1049. DOI: 10.1016/j.mechmat.2009.04.011
- Qing, H., and Mishnaevsky, L. (2009b) "Moisture-related mechanical properties of softwood: 3D micromechanical modelling," *Comput. Mater. Sci.* 46(2), 310-320. DOI: 10.1016/j.commatsci.2009.03.008
- Rasband, W. S. (2012). *ImageJ*, U.S. National Institutes of Health, Bethesda, MD.
- Salmén, L. (2004). "Micromechanical understanding of the cell-wall structure," *C. R. Biol.* 327(9-10), 873-880. DOI: 10.1016/j.crvi.2004.03.010
- Shamsudin, S., Md-Shah, U. K., Zainudin, H., Abd-Aziz, S., Mustapa-Kama, S. M., Shirai, Y., and Hassan, M. A. (2012). "Effect of steam pretreatment on oil palm empty fruit bunch for the production of sugars," *Biomass Bioenerg.* 36, 280-288. DOI: 10.1016/j.biombioe.2011.10.040
- Shuit, S. H., Tan, K. T., Lee, K. T., and Kamaruddin, A. H. (2009). "Oil palm biomass as a sustainable energy source: A Malaysian case study," *Energy* 34(9), 1225-1235. DOI: 10.1016/j.energy.2009.05.008
- Song, K., Davila, C. G., and Rose, C. A. (2008). "Guidelines and parameter selection for the simulation of progressive delamination," *ABAQUS User's Conference*, Newport, RI.
- Sreekala, M. S., Kumaran, M. G. and Thomas, S. (1997). "Oil palm fibers: Morphology, chemical composition, surface modification, and mechanical properties," *J. Appl. Polym. Sci.* 66(5), 821-835. DOI: 10.1002/(SICI)1097-4628(19971031)66:5<821::AID-APP2>3.0.CO;2-X
- Yunos, N. S. H., Baharuddin, A. S., Md-Yunos, K. F., Naim, M. N., and Nishida, H. (2012). "Physicochemical property changes of oil palm mesocarp fibers treated with high pressure steam," *BioResources* 7(4), 5983-5994.
- Yusoff, M. Z. M., Salit, M. S., and Ismail, N. (2009). "Tensile properties of single oil palm empty fruit bunch (OPEFB) fibre," *Sains Malays.* 38(4), 525-529.

Article submitted: June 17, 2014; Peer review completed: September 27, 2014; Revised version received and accepted: September 30, 2014; Published: October 7, 2014.